

MegaSaM: Accurate, Fast, and Robust Structure and Motion from Casual Dynamic Videos

Zhengqi Li¹ Richard Tucker¹ Forrester Cole¹ Qianqian Wang^{1,2} Linyi Jin^{1,3}
 Vickie Ye² Angjoo Kanazawa² Aleksander Holynski^{1,2} Noah Snavely¹

¹Google DeepMind ²UC Berkeley ³University of Michigan

Abstract

We present a system that allows for accurate, fast, and robust estimation of camera parameters and depth maps from casual monocular videos of dynamic scenes. Most conventional structure from motion and monocular SLAM techniques assume input videos that feature predominantly static scenes with large amounts of parallax. Such methods tend to produce erroneous estimates in the absence of these conditions. Recent neural network-based approaches attempt to overcome these challenges; however, such methods are either computationally expensive or brittle when run on dynamic videos with uncontrolled camera motion or unknown field of view. We demonstrate the surprising effectiveness of a deep visual SLAM framework: with careful modifications to its training and inference schemes, this system can scale to real-world videos of complex dynamic scenes with unconstrained camera paths, including videos with little camera parallax. Extensive experiments on both synthetic and real videos demonstrate that our system is significantly more accurate and robust at camera pose and depth estimation when compared with prior and concurrent work, with faster or comparable running times. See interactive results on our project page: mega-sam.github.io.

1. Introduction

Extracting camera parameters and scene geometry from a set of images is a fundamental problem in computer vision, commonly referred to as structure from motion (SfM) or Simultaneous Localization and Mapping (SLAM). While decades of research have yielded mature algorithms for stationary scenes with large camera baselines, these methods often falter when applied to casual monocular videos captured in uncontrolled setting [26, 79]. Such videos, frequently captured by handheld cameras, typically exhibit limited camera motion parallax (e.g., nearly stationary or rotational cameras) and a broad range of focal lengths, and often include moving objects and scene dynamics. Recent

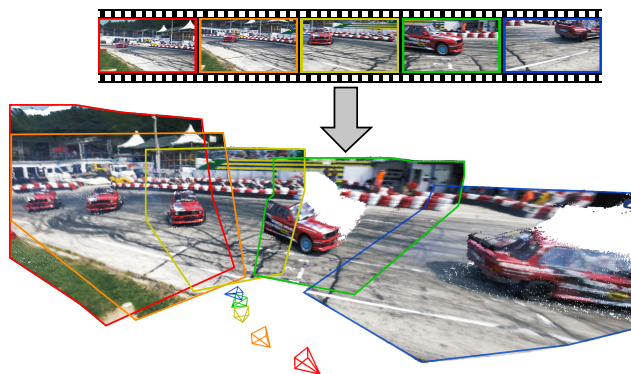


Figure 1. **MegaSaM** enables accurate, fast and robust estimation of cameras and scene structure from a casually captured monocular video of a dynamic scene. Top: input video frames (every tenth frame shown). Bottom: our estimated camera and 3D point clouds unprojected by predicted video depths without any postprocessing.

efforts to address these challenges have focused on two primary strategies: optimizing camera and scene geometry by fine-tuning mono-depth networks or reconstructing radiance fields [35, 36, 78, 79]; or combining intermediate estimates derived from monocular video, such as depth, flows, long-term trajectory and motion segmentation, into a global optimization framework [6, 26, 35, 77, 80]. However, these approaches are computational expensive or brittle when applied to unconstrained videos that feature long time duration, unconstrained camera paths, or complex scene dynamics.

In this work, we present MegaSaM, a full pipeline for *accurate, fast and robust* camera tracking and depth estimation from in-the-wild monocular videos of dynamic scenes. Our approach combines the strengths of several prior works, leading to results with previously unachievable quality, as shown in Fig. 1. In particular, we reexamine and extend prior deep visual SLAM framework for camera tracking. A defining feature of deep visual SLAM systems like DROID-SLAM [60] is that they adopt a differentiable bundle adjustment (BA) layer that iteratively updates scene geometry and camera

pose variables, and intermediate predictions are learned from large amounts of data through camera and flow supervision. We find that such a learned layer is critical for achieving accurate and efficient camera pose estimation for the more challenging case of dynamic video. Building on this foundation, one of our key innovations for handling dynamic scene is to integrate monocular depth priors and motion probability maps into a differentiable SLAM paradigm.

Further, we analyze the observability of structure and camera parameters in the video and introduce an uncertainty-aware global BA scheme, which improves system robustness when camera parameters are poorly constrained by the input video. We also demonstrate how consistent video depths can be accurately and efficiently obtained without the need for test-time network fine-tuning. Extensive evaluation on synthetic and real-world datasets demonstrates that our system significantly outperforms prior and concurrent baselines in both camera and depth estimation accuracy, while achieving competitive or superior runtime performance.

2. Related Work

Visual SLAM and SfM. SLAM and SfM are used to estimate camera parameters and 3D scene structure from video sequences or unstructured image collections. Conventional approaches tackle this problem by first estimating 2D correspondence between images through feature matching [1, 5, 8, 25, 38, 45, 46, 52, 56, 57] or photometric alignment [9, 10, 39]. They then optimize 3D point locations and camera parameters by minimizing reprojection or photo-consistency errors through bundle adjustment (BA) [62].

Recently, deep visual SLAM and SfM systems have emerged that adopt deep neural networks to estimate pairwise or long-term correspondences [2, 7, 18, 19, 21, 55, 58, 60, 61, 64, 66, 74], to reconstruct radiance fields [11, 34, 42] or global 3D point clouds [28, 67]. While these methods demonstrate accurate camera tracking and reconstruction, they typically assume predominantly static scenes and sufficient camera baselines between frames. Therefore, their performance can degrade significantly or fail entirely in the presence of scene dynamics or limited camera parallax.

Several recent works share similar goals with ours in addressing these limitations. Robust-CVD [29] and CasualSAM [79] jointly estimate camera parameters and dense depth maps from dynamic videos by optimizing a spatially varying spline or fine-tuning monocular depth networks. Particle-SfM [80] and LEAP-VO [6] first infer moving object masks based on long-range trajectories, then use this information to downweight the contribution of the features during bundle adjustment. Concurrent work, MonST3R [77], adopts a 3D point cloud representation from DuST3R [67] and localizes cameras via an additional alignment optimization. Our approach shares similar ideas, but we show that performance can be significantly improved by coupling the

differentiable SLAM system with the intermediate predictions of underlying dynamic scenes.

Monocular depth. Recent work on monocular depth prediction has shown strong generalization on in-the-wild single images by training deep neural networks on large amounts of synthetic and real-world data [13, 22, 30, 31, 44, 47, 48, 50, 72, 73, 75, 76]. However, these single-image models tend to produce temporally inconsistent depth from videos. To overcome this issue, prior techniques propose to fine-tune monodepth models by performing test-time optimization [36, 78] or to use transformer or diffusion models to directly predict video depths [20, 54, 70]. Our approach follows the spirit of the first paradigm, but we show that we can achieve better video depth quality without resorting to expensive network fine-tuning for every video.

Dynamic scene reconstruction. Several recent works have adopted time-varying radiance field representations to perform dynamic scene reconstruction and novel view synthesis from in-the-wild videos [12, 27, 32, 33, 35, 40, 41, 65, 68, 71]. Our work is orthogonal to most of these techniques since most radiance field reconstruction methods require camera parameters or video depth maps as inputs, and our outputs can be used as inputs to these systems.

3. MegaSaM

Given an unconstrained, continuous video sequence $\mathcal{V} = \{I_i \in \mathcal{R}^{H \times W}\}_{i=1}^N$ our goal is to estimate camera poses $\hat{\mathbf{G}}_i \in SE(3)$, focal length \hat{f} (if unknown), and dense video depth maps $\mathcal{D} = \{\hat{D}_i\}_{i=1}^N$. Our approach does not pose any constraints on the camera and object motions present in the input video. Our camera tracking and video depth estimation modules build upon prior deep visual SLAM (in particular, DROID-SLAM [60]) and casual structure and motion [79] frameworks, respectively.

In the following section, we first summarize the key components of a deep visual SLAM framework designed for tracking videos of static scenes with sufficient camera motion parallax (Sec. 3.1). We then introduce key modifications to this framework, at both the training and inference stages, that enable fast, robust and accurate camera tracking for unconstrained dynamic videos (Sec. 3.2). Finally, we demonstrate how to efficiently estimate consistent video depths given the estimated camera parameters (Sec. 3.3).

3.1. Deep visual SLAM formulation

Deep visual SLAM systems like DROID-SLAM [60] are characterized by a differentiable, learned bundle adjustment (BA) layer that iteratively updates structure and motion parameters. In particular, they keep track of two state variables while processing a video: a per-frame low-resolution disparity map $\hat{\mathbf{d}}_i \in \mathcal{R}^{\frac{H}{8} \times \frac{W}{8}}$, and camera poses $\hat{\mathbf{G}}_i \in SE(3)$. These variables are updated iteratively during both training

and inference stages through the differentiable BA layer, which operates over a set of image pairs from a frame-graph $(I_i, I_j) \in \mathcal{P}$, built dynamically to connect frames with overlapping field of view.

Given two video frames I_i and I_j from the frame graph as input, DROID-SLAM learns to predict a 2D correspondence field $\hat{\mathbf{u}}_{ij} \in \mathcal{R}^{\frac{H}{8} \times \frac{W}{8} \times 2}$ and a confidence $\hat{\mathbf{w}}_{ij} \in \mathcal{R}^{\frac{H}{8} \times \frac{W}{8}}$ through convolutional gated recurrent units in an iterative manner: $(\hat{\mathbf{u}}_{ij}^{k+1}, \hat{\mathbf{w}}_{ij}^{k+1}) = F(I_i, I_j, \hat{\mathbf{u}}_{ij}^k, \hat{\mathbf{w}}_{ij}^k)$, where k denotes the k^{th} iteration. In addition, the rigid-motion correspondence field can also be derived from the camera ego-motion and the disparity through a multi-view constraint:

$$\mathbf{u}_{ij} = \pi \left(\hat{\mathbf{G}}_{ij} \circ \pi^{-1}(\mathbf{p}_i, \hat{\mathbf{d}}_i, K^{-1}), K \right), \quad (1)$$

where \mathbf{p}_i denotes a grid of pixel coordinates, π denotes the perspective projection operator, $\hat{\mathbf{G}}_{ij} = \hat{\mathbf{G}}_j \circ \hat{\mathbf{G}}_i^{-1}$ is the relative camera pose between I_i and I_j , and $K \in \mathcal{R}^{3 \times 3}$ denotes the camera intrinsic matrix.

Differentiable bundle adjustment. DROID-SLAM assumes known focal length, but focal length is typically not known a priori for in-the-wild videos. Therefore, we optimize camera poses, focal length and disparity by iteratively minimizing a weighted reprojection cost between the current flows predicted by the network and the rigid-motion ones derived from camera parameters and disparity [16]:

$$\mathcal{L}(\hat{\mathbf{G}}, \hat{\mathbf{d}}, \hat{f}) = \sum_{(i,j) \in \mathcal{P}} \|\hat{\mathbf{u}}_{ij} - \mathbf{u}_{ij}\|_{\Sigma_{ij}}^2 \quad (2)$$

where weights $\Sigma_{ij} = \text{diag}(\hat{\mathbf{w}}_{ij})^{-1}$. To enable differentiable end-to-end training, we perform optimization of Eq. 2 with the Levenberg–Marquardt algorithm:

$$(\mathbf{J}^T \mathbf{W} \mathbf{J} + \lambda \text{diag}(\mathbf{J}^T \mathbf{W} \mathbf{J})) \Delta \xi = \mathbf{J}^T \mathbf{W} \mathbf{r} \quad (3)$$

where $\Delta \xi = (\Delta \mathbf{G}, \Delta \mathbf{d}, \Delta f)^T$ is the parameter updates of the state variables, \mathbf{J} is the Jacobian of reprojection residuals w.r.t. the parameters, and \mathbf{W} is a diagonal matrix containing $\hat{\mathbf{w}}_{ij}$ from each frame pair. λ is a damping factor predicted by the network during each BA iteration. We can separate camera parameters (including poses and focal length) and disparity variables by dividing the approximated Hessian on the LHS of Eq. 3 into following block matrix form:

$$\begin{bmatrix} \mathbf{H}_{\mathbf{G},f} & \mathbf{E}_{\mathbf{G},f} \\ \mathbf{E}_{\mathbf{G},f}^T & \mathbf{H}_{\mathbf{d}} \end{bmatrix} \begin{bmatrix} \Delta \xi_{\mathbf{G},f} \\ \Delta \mathbf{d} \end{bmatrix} = \begin{bmatrix} \tilde{\mathbf{r}}_{\mathbf{G},f} \\ \tilde{\mathbf{r}}_{\mathbf{d}} \end{bmatrix} \quad (4)$$

Since only a single disparity variable is included in each pairwise reprojection term from Eq. 2, $\mathbf{H}_{\mathbf{d}}$ in Eq. 4 is a diagonal matrix, and hence we can efficiently compute parameter updates using the Schur complement trick [62], which leads to fully differentiable BA update:

$$\Delta \xi_{\mathbf{G},f} = \left[\mathbf{H}_{\mathbf{G},f} - \mathbf{E}_{\mathbf{G},f} \mathbf{H}_{\mathbf{d}}^{-1} \mathbf{E}_{\mathbf{G},f}^T \right]^{-1} (\tilde{\mathbf{r}}_{\mathbf{G},f} - \mathbf{E}_{\mathbf{G},f} \mathbf{H}_{\mathbf{d}}^{-1} \tilde{\mathbf{r}}_{\mathbf{d}}) \quad (5)$$

$$\Delta \mathbf{z} = \mathbf{H}_{\mathbf{d}}^{-1} (\tilde{\mathbf{r}}_{\mathbf{d}} - \mathbf{E}_{\mathbf{G},f}^T \Delta \xi_{\mathbf{G},f}) \quad (6)$$



Figure 2. **Learned movement map.** Left: input video frame, right: corresponding learned motion probability map.

Training. The flow and uncertainty predictions are trained end-to-end from a collection of synthetic video sequences of static scenes:

$$\mathcal{L}_{\text{static}} = \mathcal{L}_{\text{cam}} + w_{\text{flow}} \mathcal{L}_{\text{flow}} \quad (7)$$

where \mathcal{L}_{cam} and $\mathcal{L}_{\text{flow}}$ are losses comparing estimated camera parameters and ego-motion induced flows from the BA layer with corresponding ground truths.

3.2. Scaling to in-the-wild dynamic videos

Deep Visual SLAM works reasonably well for videos that feature static scenes and have sufficient camera translation, but its performance degrades when operating on videos of dynamic content, or videos with limited parallax, as shown in the first column of Fig. 3. To overcome these issues, we propose key modifications to the original training and inference pipeline. First, our model predicts object movement maps that are learned together with flow and uncertainty in order to downweight dynamic elements within the differentiable BA layer. Second, we propose to integrate priors from mono-depth estimates into the both training and inference pipeline, and perform uncertainty-aware global BA, both of which aid disambiguation of object and camera motion in challenging casual dynamic videos. Our system is trained on synthetic data alone, but we demonstrate its strong generalization to real-world videos.

3.2.1 Training

Learning motion probability. Recall from Sec. 3.1 that for every selected image pair $(I_i, I_j) \in \mathcal{P}$, our model predicts a 2D flow $\hat{\mathbf{u}}_{ij}$ and associated confidence $\hat{\mathbf{w}}_{ij}$ at each BA iteration, and that these predictions are supervised from synthetic sequences of static scenes. To extend the model to handle dynamic scenes, we can directly train the model predictions on videos of dynamic scenes with corresponding ground truth supervision, hoping that the pairwise uncertainty will subsume the object motion information automatically during training. However, we find that this simple training strategy tends to produce suboptimal results due to unstable training behaviour from differentiable BA layers.

Instead, we propose to use an additional network F_m to iteratively predict an *object movement probability map* $\mathbf{m}_i \in \mathcal{R}^{\frac{H}{8} \times \frac{W}{8}} = F_m(\{I_i\} \cup \mathcal{N}(i))$ conditioned on I_i and a set of its neighboring keyframes $\mathcal{N}(i) = \{I_j | (i, j) \in \mathcal{P}\}$. This movement map is specifically supervised to predict pixels that correspond to dynamic content based on multi-frame information. During each BA iteration, we combine pairwise flow confidence $\hat{\mathbf{w}}_{ij}$ with object movement map \mathbf{m}_i to form the final weights in Eq. 2: $\tilde{\mathbf{w}}_{ij} = \hat{\mathbf{w}}_{ij} \mathbf{m}_i$.

Moreover, we design a two-stage training scheme that trains the models on a mixture of static and dynamic videos to effectively learn 2D flows along with the movement probability maps. In the first *ego-motion pretraining* stage, we train the original deep SLAM model F by supervising the predicted flows and confidence maps (using the losses in Eq. 7) with synthetic data of static scenes, *i.e.*, without any dynamic video data. This stage helps model effectively learn pairwise flows and corresponding confidence induced only by ego-motion. In the second *dynamic fine-tuning* stage, we freeze the parameters of F and finetune F_m on synthetic dynamic videos, conditioning F_m on the features from our pretrained F during each iteration to predict movement probability map \mathbf{m}_i , supervising through both camera and cross-entropy losses:

$$\mathcal{L}_{\text{dynamic}} = \mathcal{L}_{\text{cam}} + w_{\text{motion}} \mathcal{L}_{\text{CE}} \quad (8)$$

This stage decorrelates learning scene dynamics from learning 2D correspondences, and thus leads to more stable and effective training behavior for the differentiable BA framework. We found this training scheme to be critical for producing accurate camera estimation results for dynamic videos, as shown in our ablation study. We visualize learned motion probability maps \mathbf{m}_i in Fig. 2.

Disparity and camera initialization. DROID-SLAM initializes disparity $\hat{\mathbf{d}}$ by simply setting it to a constant value of 1. However, we find that this initialization fails to perform accurate camera tracking on videos with limited camera baselines and complex scene dynamics. Inspired by recent work [32, 33, 35, 65], during both the training and inference stages, we perform data-driven initialization by integrating a mono-depth prior. During training, we initialize $\hat{\mathbf{d}}$ with disparity from DepthAnything [72] with the estimated global scale and shift borrowed from the ground truth depth of each training sequence. For each training sequence, we initialize first two camera poses to the ground-truth to remove the gauge ambiguity, and initialize the camera focal length by randomly perturbing the ground truth value by 25%.

3.2.2 Inference

Our inference pipeline consists of two components: (i) a frontend module registers cameras for keyframes by performing frame selection followed by a sliding window BA.

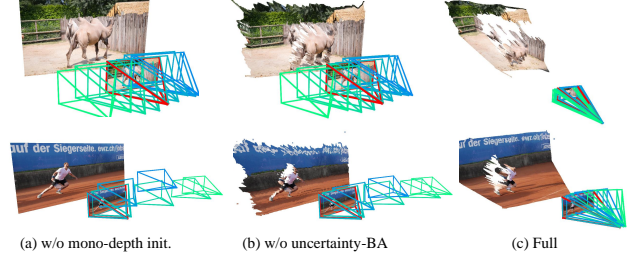


Figure 3. **Ablation on our design choices.** From left to right, we visualize cameras and reconstruction from our system (a) without mono-depth initialization, (b) without uncertainty-aware BA, (c) with full configuration. For these difficult near-rotational sequences, our full method produces much better camera and scene geometry.

(ii) a backend module refines the estimates by performing global BA over all video frames. In this subsection, we describe the modifications we made at inference.

Initialization and frontend tracking. Similar to training, we incorporate both mono-depth and focal length predictions into the inference pipeline. In particular, we initialize per-frame disparity maps $\hat{\mathbf{d}}_i$ with metric aligned monocular disparity $D_i^{\text{align}} = \hat{\alpha} D_i^{\text{rel}} + \hat{\beta}$, where D_i^{rel} is per-frame affine-invariant disparity from [72], and per-video global scale and shift parameters $(\hat{\alpha}, \hat{\beta})$ are estimated through median aligning D_i^{rel} with an additional metric depth estimates D_i^{abs} from UniDepth [44]: $\hat{\alpha}_i = \frac{D_i^{\text{abs}} - \text{median}_i(D_i^{\text{abs}})}{D_i^{\text{rel}} - \text{median}(D_i^{\text{rel}})}$; $\hat{\beta} = \text{median}(D_i^{\text{abs}} - \hat{\alpha} D_i^{\text{rel}})$.¹ The UniDepth model also predicts the focal length of each frame; we use the median estimate across the video frames to obtain an initial focal length estimate \hat{f} , which is fixed within the frontend stage.

To initialize the SLAM system, we accumulate keyframes with sufficient pairwise motion until we have a set of $N_{\text{init}} = 8$ active images. We initialize camera poses for these keyframes by performing camera motion-only bundle adjustment while fixing disparity variables $\hat{\mathbf{d}}_i$ to aligned monocular disparity D_i^{align} . After initialization, we incrementally add new keyframes, remove old keyframes, and perform local BA in a sliding window manner, where each keyframe disparity is also initialized to aligned mono-disparity. In this stage, the BA cost function consists of a reprojection error and a mono-depth regularization term:

$$\mathcal{C} = \sum_{(i,j) \in \mathcal{P}} \|\hat{\mathbf{u}}_{ij} - \mathbf{u}_{ij}\|_{\Sigma_{ij}}^2 + w_d \sum_i \|\hat{\mathbf{d}}_i - D_i^{\text{align}}\|^2. \quad (9)$$

Uncertainty-aware global BA. The backend module first performs global BA over all keyframes. The module then performs a pose-graph optimization to register the poses of

¹We combine two mono-depth models since they have complementary advantages: DepthAnything provides more accurate and consistent depths, whereas UniDepth provides scene scale and shift estimates.



Figure 4. **Visualization of epistemic uncertainty.** From left to right, we visualize camera paths, reference image and corresponding epistemic uncertainty of disparity. The geometry is not observable from the top example with little camera parallax, as indicated by the larger uncertainty. The peak on the bottom uncertainty map corresponds to the epipole for forward moving motion.

non-keyframes. Finally, the backend module refines the entire camera trajectory via a global BA over all video frames.

This design raises a question: should we (or when should we) add mono-depth regularization from Eq. 9 into the global bundle adjustment? One on hand, if there is sufficient camera baseline in the input video, we observe that mono-depth regularization isn’t needed, since the problem is already well-constrained and in fact the error from mono-depth can diminish camera tracking accuracy. On the other hand, if a video is captured from a rotational camera with little camera baseline, then performing a reprojection-only BA without additional constraints can lead to degenerate solutions, as shown in the second column of Fig. 3.

To see why, we explore the approximate Hessian matrix from the linear system in Eq. 4. As shown by Goli *et al.* [14], given the posterior, $p(\theta|\mathcal{I})$, we can use Laplace approximations to estimate the covariance Σ of the variables through the inverse Hessian: $\Sigma_\theta = -\mathbf{H}(\theta^*)^{-1}$, where θ^* is the MAP estimate of the parameters and Σ_θ denotes the epistemic uncertainty of estimated variables [23]. Since inverting the full Hessian is computationally expensive when the number of input frames is large, we follow Ritter *et al.* [49] and approximate Σ_θ through the diagonal of the Hessian:

$$\Sigma_\theta \approx \text{diag}(-\mathbf{H}(\theta^*))^{-1} \quad (10)$$

Intuitively, when we consider the reprojection error in Eq. 2, the Jacobian of estimated variables \mathbf{J}_θ indicates how much the reprojection error would change if we perturb the variables. Therefore, the uncertainty Σ_θ is large when perturbing the parameters has little impact on the reprojection error. Specifically, let us consider the disparity variables, and consider an extreme case where the input video is captured by a static camera. In this case, the pairwise reprojection error would be unchanged as a function of disparity, implying a large uncertainty in the estimated disparity; that is, the disparity is unobservable from the video alone. We visualize

the spatial uncertainty of the estimated normalized disparity Σ_d in Fig 4: the first row shows a video featuring rotational dominant motion, whereas the second row shows videos captured by a forward-moving camera. From the color bars in the third column, we see the range of disparity uncertainty Σ_d is much higher in the first example.

Such uncertainty quantification gives us a measure for observability of camera and disparity parameters, allowing us to decide where we should add mono-depth regularization (and additionally when we should turn off camera focal length optimization). In practice, we find that simply checking the median uncertainty of normalized disparity and uncertainty of normalized focal length works well for all the videos we tested. In particular, after completing front-end tracking, we retrieve the diagonal entry of disparity Hessian formed from all the keyframes and compute its median $\text{med}(\text{diag}(\mathbf{H}_d))$, as well as the Hessian entry of the shared focal length H_f . We then set the mono-depth regularization weight based on the median disparity Hessian $w_d = \gamma_d \exp(-\beta_d \text{med}(\text{diag}(\mathbf{H}_d)))$. In other words, we enable mono-depth regularization if the camera poses are unobservable from the input video alone due to limited camera motion parallax. In addition, we disable focal length optimization if $H_f < \tau_f$, since this condition indicates that focal length is likely unobservable from the input.

3.3. Consistent depth optimization

Optionally, one can obtain more accurate and consistent video depth at higher resolution than the estimated low-res disparity variables given the estimated camera parameters.

In particular, we follow CasualSAM [79] and perform an additional first-order optimization on video depths along with per-frame aleatoric uncertainty maps. Our objective consist of three cost functions:

$$\mathcal{C}_{\text{cvd}} = w_{\text{flow}}\mathcal{C}_{\text{flow}} + w_{\text{temp}}\mathcal{C}_{\text{temp}} + w_{\text{prior}}\mathcal{C}_{\text{prior}} \quad (11)$$

where $\mathcal{C}_{\text{flow}}$ denotes pairwise 2D flow reprojection loss, $\mathcal{C}_{\text{temp}}$ is temporal depth consistency loss, and $\mathcal{C}_{\text{prior}}$ is scale invariant mono-depth prior loss. We derive 2D optical flow at the original frame resolution from an off-the-shelf module [59].

Note that our design has a few differences compared to CasualSAM: (i) instead of performing a time-consuming mono-depth network fine-tuning, we construct and optimize a sequence of variables for disparity and uncertainty over the input video; (ii) we fix camera parameters instead of jointly optimizing cameras and depths during optimization; (iii) we adopt surface normal consistency and multi-scale depth gradient matching losses [30, 51] to replace the depth prior loss used in CasualSAM [79]. We find that these modifications lead to much faster optimization times as well as more accurate video depth estimates. We refer readers see the supplementary material for more details of our losses and optimization scheme.

Method	Calibrated			Uncalibrated			Time
	ATE	RTE	RRE	ATE	RTE	RRE	
CasualSAM [79]	0.036	0.013	0.20	0.067	0.019	0.47	1.6m
LEAP-VO [6]	0.041	0.023	0.17	-	-	-	1.3s
ACE-Zero [3]	0.053	0.028	0.30	0.065	0.028	1.92	10s
Particle-SfM [80]	0.062	0.032	1.26	0.057	0.038	1.64	21s
RoDynRF [35]	0.110	0.049	1.68	0.109	0.051	1.32	15m
MonST3R [77]	-	-	-	0.078	0.038	0.49	1.0s
Ours	0.018	0.008	0.04	0.023	0.008	0.06	1.0s

Table 1. Quantitative comparisons of camera estimation on the Sintel dataset.

Method	Calibrated			Uncalibrated			Time
	ATE	RTE	RRE	ATE	RTE	RRE	
CasualSAM [79]	0.185	0.022	0.23	0.209	0.027	0.28	2.8m
LEAP-VO [6]	0.167	0.011	0.09	-	-	-	0.8s
ACE-Zero [3]	0.062	0.012	0.11	0.056	0.012	0.12	1.6s
Particle-SfM [80]	0.081	0.014	0.20	0.087	0.015	0.29	35s
RoDynRF [35]	0.548	0.074	0.70	0.562	0.087	0.90	6.6m
MonST3R [77]	-	-	-	0.690	0.078	0.54	1.0s
Ours	0.020	0.005	0.05	0.020	0.005	0.06	0.8s

Table 2. Quantitative comparisons of camera estimation on the DyCheck dataset.

4. Experiments

Implementation details. In our two-stage training scheme, we first pretrain our model on synthetic data of static scenes, which include 163 scenes from TartanAir [69] and 5K videos from static Kubric [15]. In the second stage, we finetune motion module F_m on 11K dynamic videos from Kubric [15]. Each training example consists of a 7-frame video sequence. We set $w_{\text{flow}} = 0.02$, $w_{\text{motion}} = 0.1$ during training. Training the camera tracking module using the Adam optimizer [24] takes around 4 days with 8 Nvidia 80G A100s. Within the initialization and frontend phase, we set mono-depth regularization weight $w_d = 0.05$. In the backend phase, we set $\gamma_d = 1 \times 10^{-4}$, $\beta_d = 0.05$, $\tau_f = 50$. In term of consistent video depth optimization, we set $w_{\text{flow}} = w_{\text{prior}} = 1.0$, $w_{\text{temp}} = 0.2$. The average running time of our optimization is 1.3 FPS for video depths at resolution 336×144 on Sintel, but we visualize and evaluate them at resolution of 672×288 . We refer readers to supplemental material for more details of network architectures, and other training/inference settings.

Baseline. We compare MegaSaM to recent camera pose estimation methods on both calibrated (known focal length) and uncalibrated (unknown focal length) videos. ACE-Zero [3] is a state-of-the-art camera localization method based on scene coordinate regression, designed for static scenes. CasualSAM [79] and RoDynRF [35] jointly estimate camera parameters and dense scene geometry through optimizing mono-

Method	Calibrated			Uncalibrated			Time
	ATE	RTE	RRE	ATE	RTE	RRE	
CasualSAM [79]	0.031	0.005	0.31	0.035	0.005	0.30	1.1m
LEAP-VO [6]	0.016	0.004	0.04	-	-	-	0.6s
ACE-Zero [3]	0.091	0.008	0.08	0.091	0.008	0.09	4.0s
Particle-SfM [80]	0.051	0.007	0.10	0.054	0.007	0.14	49s
RoDynRF [35]	0.116	0.021	0.34	0.112	0.031	0.39	7.6m
MonST3R [77]	-	-	-	0.073	0.014	0.18	1.7s
Ours	0.004	0.001	0.02	0.004	0.001	0.02	0.7s

Table 3. Quantitative comparisons of camera estimation on a dataset of In-the-Wild footage.

Method	Sintel [4]			Dycheck [12]		
	abs-rel	log-rmse	$\delta_{1.25}$	abs-rel	log-rmse	$\delta_{1.25}$
DA-v2 [73]	0.37	0.55	58.6	0.20	0.27	84.7
DepthCrafter [20]	0.27	0.50	68.2	0.22	0.29	83.7
CasualSAM [79]	0.31	0.49	64.2	0.21	0.30	78.4
MonST3R [77]	0.31	0.43	62.5	0.26	0.35	66.5
Ours	0.21	0.39	73.1	0.11	0.20	94.1

Table 4. **Quantitative comparisons of video depths.** Lower is better for abs-rel and log-rmse, and higher is better for $\delta_{1.25}$.

depth networks or instant-NGP [37]. Particle-SfM [80] and LEAP-VO [6] estimate cameras from dynamic videos by predicting motion segmentation from long-term trajectories, then using them to mask out moving objects within a standard visual odometry or SfM pipeline. The concurrent work MonST3R [77] extends Dust3R [67] to handle dynamic scenes, estimating camera parameters from global 3D point clouds predicted from pairs of input frames. To evaluate depth accuracy, we compare our outputs to those from CasualSAM, MonST3R, and VideoCrafter [20]. We also include raw mono-depth from DepthAnything-V2 [73] for the sake of completeness. We run all the above baselines using their respective open-source implementations on the same machine with single Nvidia A100 GPU.

4.1. Benchmarks and metrics

MPI Sintel. The MPI Sintel [4] dataset includes animated video sequences consisting of complex object motions and camera paths. Following CasualSAM [79], we evaluate all methods on the 18 sequences from the dataset, each of which consists of 20-50 images.

DyCheck. The DyCheck dataset [12] was initially designed for evaluating the task of novel view synthesis, and includes real-world videos of dynamic scenes captured from hand-held cameras. Each video includes 180-500 frames. We use the refined camera parameters and sensor depths provided by Shape of Motion [65] as ground truth.

In-the-wild. We further evaluate on in-the-wild dynamic videos. Specifically, we include comparisons on 12 in-the-

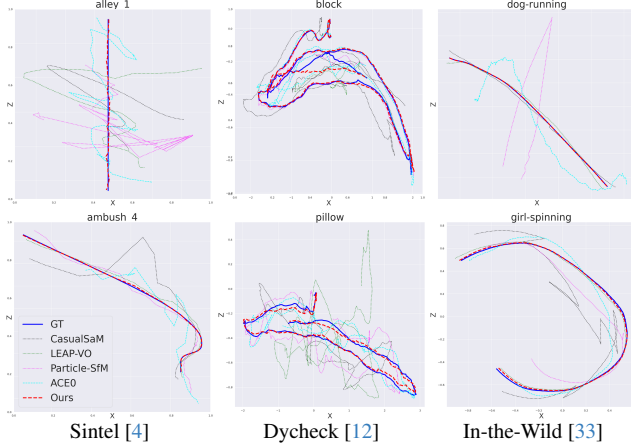


Figure 5. **Visualization of estimated camera trajectories.** Due to scene dynamics, our camera estimate (red dash) deviates less from the ground truth camera trajectory (blue solid line) than all other baselines.

wild videos used by DynIBaR [33]. These videos feature long time duration (100-600 frames), uncontrolled camera paths, and complex scene motions. We construct ground truth movement masks via instance segmentation [17], where the instance IDs are manually specified, and use them to mask out moving objects before running COLMAP [52] to obtain reliable camera parameters.

Metrics. We use standard error metrics to evaluate camera pose estimation: Absolute Translation Error (ATE), Relative Translation Error (RTE), and Relative Rotation Error (RRE). Following CasualSaM, we normalize ground truth camera trajectories to be unit length, since camera tracks in different videos can vary significantly, and videos with longer trajectories can have higher influence on the computed metrics. For all methods, we align estimated camera paths to the ground truth trajectory by computing a global Sim(3) transformation via Umeyama alignment [63]. We report the average running time by dividing total running time of each method by the number of input frames. Additionally, we compare the quality of estimated video depths to recent baselines, adopting standard depth metrics: Absolute Relative Error, log RMSE, and Delta accuracy. We follow the standard evaluation protocol by excluding points that are further than 100 meters. For all methods, we align predicted video depths with ground truth through a global scale and shift estimate.

4.2. Quantitative Comparisons

Numerical results for camera pose estimation on the three benchmarks are reported in Tables 1, 2, and 3. Our approach demonstrates significant improvement and achieves the best camera tracking accuracy on all error metrics in both the calibrated and uncalibrated setting, while being competitive in terms of running time. Notably, our approach outperforms

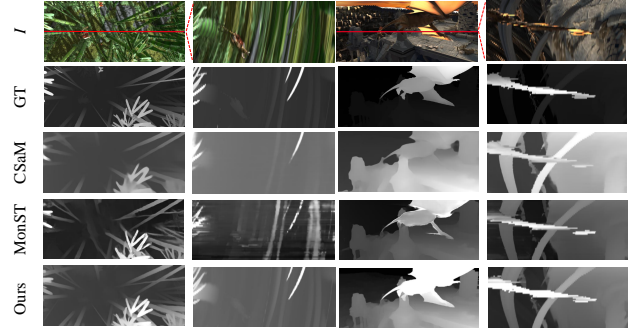


Figure 6. **Visual comparisons of video depths.** We compare video depth estimates from our approach and from CasualSaM [79] and MonST3R [77] by visualizing their depth maps (odd columns) and corresponding x - t slices (even columns).

Method	Poses			Depth	
	ATE	RTE	RRE	Abs-Rel	$\delta_{1.25}$
Droid-SLAM [60]	0.030	0.022	0.50	-	-
w/o mono-init.	0.038	0.026	0.49	-	-
w/o \hat{m}_i	0.032	0.127	0.14	-	-
w/o 2-stage train.	0.035	0.136	0.17	-	-
w/o u-BA	0.033	0.013	0.11	-	-
w/ ft-pose	0.041	0.018	0.33	0.23	71.2
w/o new \mathcal{C}_{prior}	-	-	-	0.36	72.5
Full	0.019	0.008	0.04	0.21	73.1

Table 5. **Ablation study on the Sintel dataset.** Sec. 4.3 describes each configuration.

the concurrent work MonST3R [77] in terms of both robustness and accuracy even though MonST3R adopts a more recent global 3D point cloud representation for dynamic scenes. In addition, we report results for depth prediction on the Sintel and Dycheck in Table 4. Our depth estimates again outperform other baselines significantly in all metrics.

4.3. Ablation study

We perform an ablation study to validate major design choices for our camera tracking and depth estimation modules. Specifically, we evaluate camera tracking results with different configurations: 1) vanilla Droid-SLAM [60], 2) without mono-depth initialization (w/o mono-init.), 3) without object movement map prediction (w/o \hat{m}_i), 4) directly train the model on dynamic videos without using proposed two-stage training scheme (w/o 2-stage train.), 5) always turn on mono-depth regularization during global BA (w/o u-BA). We also ablate two major design decisions for video depth estimation: 1) jointly refine camera poses and depth estimation (w/o ft-pose), and 2) use original mono-depth prior loss from CasualSaM instead of our proposed one (w/o new \mathcal{C}_{prior}). As shown in Table 5, our full system outperforms all other alternative configurations.

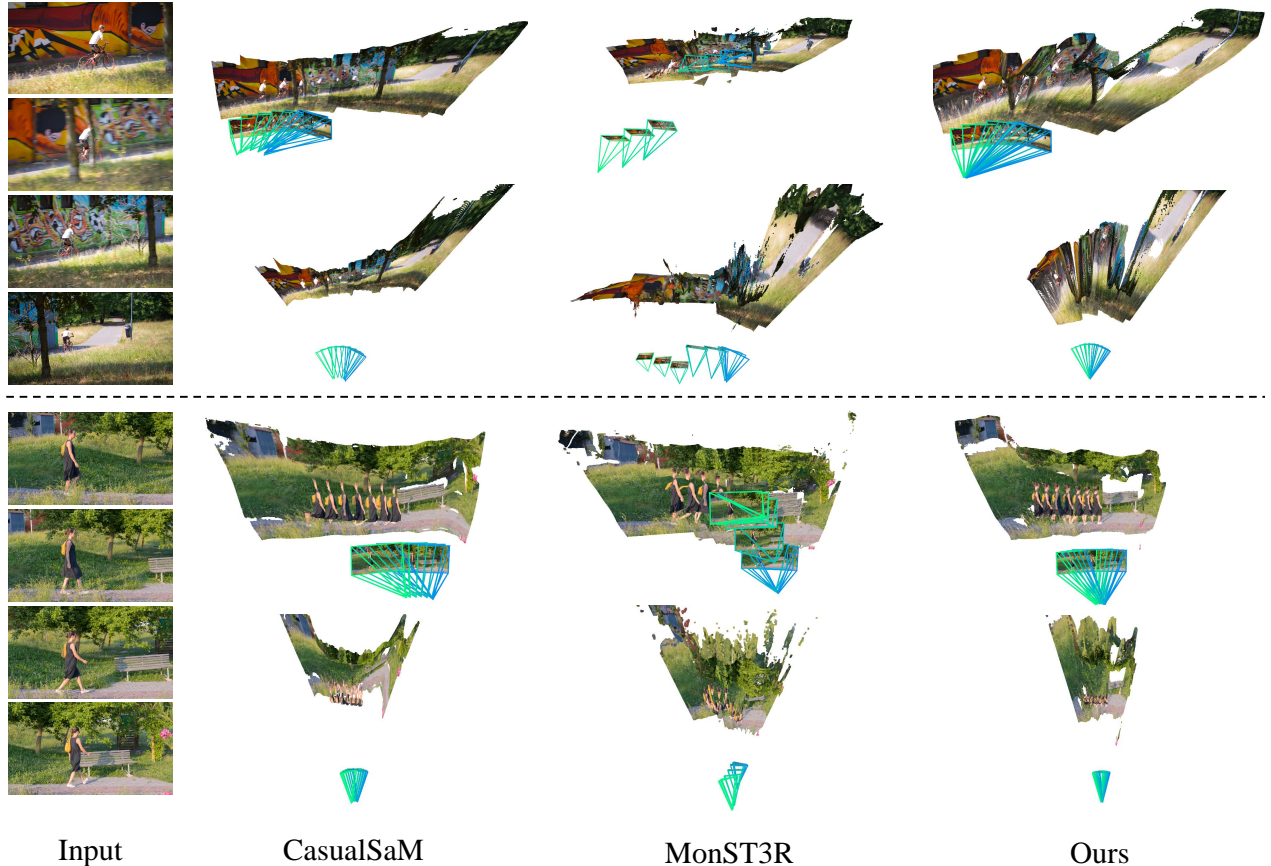


Figure 7. We visualize two examples from DAVIS with rotation-dominant camera motion and narrow FoV. Compared to CasualSAM [79] and MonST3R [77], our system produces more accurate camera and geometry estimates of underlying dynamic scenes.

4.4. Qualitative Comparisons

Fig. 5 shows qualitative comparisons of estimated camera trajectory from our method and other baselines in 2D on three benchmarks, and our camera estimates are the closest to the ground truth. Furthermore, we visualize and compare the estimated video depths from our approach and two recent optimization based techniques, CasualSAM [79] and MonST3R [77], in Fig 6. In particular, we visualize both the depth map of a reference frame and corresponding $x-t$ depth slices over the entire video. Our approach once again produces more accurate, detailed and temporally consistent video depths.

Last, we compare reconstruction and camera tracking quality among different approaches on challenging examples from DAVIS [43] by visualizing their estimated cameras and unprojected depth maps. As shown in Fig. 7, CasualSaM tends to produce distorted 3D point clouds, whereas MonST3R incorrectly treats rotational camera movement as translational one. In contrast, our approach produces more accurate camera along with more consistent geometry for such challenging inputs.

5. Discussion and conclusion

Limitations. Despite excellent performance on a variety of in-the-wild videos, we observe that our approach can fail in extremely challenging scenarios, similar to findings from prior work [79]. For instance, camera tracking fails if moving objects dominate the entire image or if there is nothing for the system to track reliably. Please see supplemental material for visualization of failure cases. Furthermore, our system cannot handle videos with varying focal lengths or strong radial distortion within the video. Incorporating better priors from current vision foundation models into the pipelines is a promising future direction to explore.

Conclusion. We presented a pipeline that produces accurate camera parameters and consistent depths from casual monocular videos of dynamic scenes. Our approach efficiently scales to in-the-wild footage of varying time duration, with unconstrained camera paths and complex scene dynamics. We have shown that, with careful extension, prior deep visual SLAM and SfM frameworks can be extended to achieve strong generalization to a broad range of videos and outperform recent state-of-the-art methods significantly.

References

- [1] Sameer Agarwal, Yasutaka Furukawa, Noah Snavely, Ian Simon, Brian Curless, Steven M Seitz, and Richard Szeliski. Building rome in a day. *Communications of the ACM*, 54(10): 105–112, 2011. [2](#)
- [2] Michael Bloesch, Jan Czarnowski, Ronald Clark, Stefan Leutenegger, and Andrew J Davison. Codeslam—learning a compact, optimisable representation for dense visual slam. In *Proceedings of the IEEE conference on computer vision and pattern recognition*, pages 2560–2568, 2018. [2](#)
- [3] Eric Brachmann, Jamie Wynn, Shuai Chen, Tommaso Cavallari, Áron Monszpart, Daniyar Turmukhambetov, and Victor Adrian Prisacariu. Scene coordinate reconstruction: Pos-ing of image collections via incremental learning of a relocal-izer. *arXiv preprint arXiv:2404.14351*, 2024. [6](#)
- [4] D. J. Butler, J. Wulff, G. B. Stanley, and M. J. Black. A naturalistic open source movie for optical flow evaluation. In *European Conf. on Computer Vision (ECCV)*, pages 611–625. Springer-Verlag, 2012. [6](#), [7](#)
- [5] Carlos Campos, Richard Elvira, Juan J Gómez Rodríguez, José MM Montiel, and Juan D Tardós. Orb-slam3: An accu-rate open-source library for visual, visual-inertial, and mul-timap slam. *IEEE Transactions on Robotics*, 37(6):1874–1890, 2021. [2](#)
- [6] Weirong Chen, Le Chen, Rui Wang, and Marc Pollefeys. Leap-vo: Long-term effective any point tracking for visual odometry. In *Proc. Computer Vision and Pattern Recognition (CVPR)*, pages 19844–19853, 2024. [1](#), [2](#), [6](#)
- [7] Jan Czarnowski, Tristan Laidlow, Ronald Clark, and An-drew J Davison. Deepfactors: Real-time probabilistic dense monocular slam. *IEEE Robotics and Automation Letters*, 5(2):721–728, 2020. [2](#)
- [8] Andrew J Davison, Ian D Reid, Nicholas D Molton, and Olivier Stasse. Monoslam: Real-time single camera slam. *IEEE transactions on pattern analysis and machine intelli-gence*, 29(6):1052–1067, 2007. [2](#)
- [9] Jakob Engel, Thomas Schöps, and Daniel Cremers. Lsd-slam: Large-scale direct monocular slam. In *European conference on computer vision*, pages 834–849. Springer, 2014. [2](#)
- [10] Jakob Engel, Vladlen Koltun, and Daniel Cremers. Direct sparse odometry. *IEEE transactions on pattern analysis and machine intelligence*, 40(3):611–625, 2017. [2](#)
- [11] Yang Fu, Sifei Liu, Amey Kulkarni, Jan Kautz, Alexei A. Efros, and Xiaolong Wang. Colmap-free 3d gaussian splatting. In *Proc. Computer Vision and Pattern Recognition (CVPR)*, pages 20796–20805, 2024. [2](#)
- [12] Hang Gao, Ruilong Li, Shubham Tulsiani, Bryan Russell, and Angjoo Kanazawa. Monocular dynamic view synthesis: A reality check. *Advances in Neural Information Processing Systems*, 35:33768–33780, 2022. [2](#), [6](#), [7](#)
- [13] Clément Godard, Oisín Mac Aodha, and Gabriel J Brostow. Unsupervised monocular depth estimation with left-right consistency. In *Proceedings of the IEEE conference on computer vision and pattern recognition*, pages 270–279, 2017. [2](#)
- [14] Lily Goli, Cody Reading, Silvia Sellán, Alec Jacobson, and Andrea Tagliasacchi. Bayes’ rays: Uncertainty quantification for neural radiance fields. In *Proc. Computer Vision and Pattern Recognition (CVPR)*, pages 20061–20070, 2024. [5](#)
- [15] Klaus Greff, Francois Belletti, Lucas Beyer, Carl Doersch, Yilun Du, Daniel Duckworth, David J Fleet, Dan Gnanapra-gasam, Florian Golemo, Charles Herrmann, Thomas Kipf, Ab-hijit Kundu, Dmitry Lagun, Issam Laradji, Hsueh-Ti (Derek) Liu, Henning Meyer, Yishu Miao, Derek Nowrouzezahrai, Cengiz Oztireli, Etienne Pot, Noha Radwan, Daniel Rebain, Sara Sabour, Mehdi S. M. Sajjadi, Matan Sela, Vincent Sitz-mann, Austin Stone, Deqing Sun, Suhani Vora, Ziyu Wang, Tianhao Wu, Kwang Moo Yi, Fangcheng Zhong, and Andrea Tagliasacchi. Kubric: a scalable dataset generator. 2022. [6](#), [14](#)
- [16] Annika Hagemann, Moritz Knorr, and Christoph Stiller. Deep geometry-aware camera self-calibration from video. In *Pro-ceedings of the IEEE/CVF International Conference on Com-puter Vision*, pages 3438–3448, 2023. [3](#)
- [17] Kaiming He, Georgia Gkioxari, Piotr Dollár, and Ross Gir-shick. Mask r-cnn. In *Proceedings of the IEEE international conference on computer vision*, pages 2961–2969, 2017. [7](#)
- [18] Xingyi He, Jiaming Sun, Yifan Wang, Sida Peng, Qixing Huang, Hujun Bao, and Xiaowei Zhou. Detector-free struc-ture from motion. In *Proceedings of the IEEE/CVF Con-ference on Computer Vision and Pattern Recognition*, pages 21594–21603, 2024. [2](#)
- [19] Aleksander Holynski, David Geraghty, Jan-Michael Frahm, Chris Sweeney, and Richard Szeliski. Reducing drift in struc-ture from motion using extended features. In *2020 Interna-tional Conference on 3D Vision (3DV)*, pages 51–60. IEEE, 2020. [2](#)
- [20] Wenbo Hu, Xiangjun Gao, Xiaoyu Li, Sijie Zhao, Xiaodong Cun, Yong Zhang, Long Quan, and Ying Shan. Depthcrafter: Generating consistent long depth sequences for open-world videos. *arXiv preprint arXiv:2409.02095*, 2024. [2](#), [6](#)
- [21] Yoni Kasten, Wuyue Lu, and Haggai Maron. Fast encoder-based 3d from casual videos via point track processing. In *The Thirty-eighth Annual Conference on Neural Information Processing Systems*. [2](#)
- [22] Bingxin Ke, Anton Obukhov, Shengyu Huang, Nando Met-zger, Rodrigo Caye Daudt, and Konrad Schindler. Repurpos-ing diffusion-based image generators for monocular depth estimation. In *Proceedings of the IEEE/CVF Conference on Computer Vision and Pattern Recognition*, pages 9492–9502, 2024. [2](#)
- [23] Alex Kendall and Yarin Gal. What uncertainties do we need in bayesian deep learning for computer vision? *Advances in neural information processing systems*, 30, 2017. [5](#), [12](#)
- [24] Diederik P. Kingma and Jimmy Ba. Adam: A method for stochastic optimization. *CoRR*, abs/1412.6980, 2014. [6](#)
- [25] Georg Klein and David Murray. Parallel tracking and map-ping for small ar workspaces. In *2007 6th IEEE and ACM international symposium on mixed and augmented reality*, pages 225–234. IEEE, 2007. [2](#)
- [26] Johannes Kopf, Xuejian Rong, and Jia-Bin Huang. Robust consistent video depth estimation. In *Proc. Computer Vision and Pattern Recognition (CVPR)*, 2021. [1](#)
- [27] Jiahui Lei, Yijia Weng, Adam Harley, Leonidas Guibas, and Kostas Daniilidis. Mosca: Dynamic gaussian fusion

- from casual videos via 4d motion scaffolds. *arXiv preprint arXiv:2405.17421*, 2024. 2
- [28] Vincent Leroy, Yann Cabon, and Jérôme Revaud. Grounding image matching in 3d with mast3r. *arXiv preprint arXiv:2406.09756*, 2024. 2
- [29] Wei Li, Qiuyin Qin, Xin Li, Ying Huangfu, Dingyi Shen, Jialing Liu, Jia Li, Bo Li, Ruixia Wu, and Xidong Duan. Robust growth of 2d transition metal dichalcogenide vertical heterostructures via ammonium-assisted cvd strategy. *Advanced Materials*, page 2408367, 2024. 2
- [30] Zhengqi Li and Noah Snavely. Megadepth: Learning single-view depth prediction from internet photos. In *Proceedings of the IEEE conference on computer vision and pattern recognition*, pages 2041–2050, 2018. 2, 5, 12
- [31] Zhengqi Li, Tali Dekel, Forrester Cole, Richard Tucker, Noah Snavely, Ce Liu, and William T Freeman. Learning the depths of moving people by watching frozen people. In *Proc. Computer Vision and Pattern Recognition (CVPR)*, pages 4521–4530, 2019. 2
- [32] Zhengqi Li, Simon Niklaus, Noah Snavely, and Oliver Wang. Neural scene flow fields for space-time view synthesis of dynamic scenes. In *Proceedings of the IEEE/CVF Conference on Computer Vision and Pattern Recognition*, pages 6498–6508, 2021. 2, 4
- [33] Zhengqi Li, Qianqian Wang, Forrester Cole, Richard Tucker, and Noah Snavely. Dynibar: Neural dynamic image-based rendering. In *Proc. Computer Vision and Pattern Recognition (CVPR)*, pages 4273–4284, 2023. 2, 4, 7
- [34] Chen-Hsuan Lin, Wei-Chiu Ma, Antonio Torralba, and Simon Lucey. Barf: Bundle-adjusting neural radiance fields. In *Proc. Computer Vision and Pattern Recognition (CVPR)*, pages 5741–5751, 2021. 2
- [35] Yu-Lun Liu, Chen Gao, Andreas Meuleman, Hung-Yu Tseng, Ayush Saraf, Changil Kim, Yung-Yu Chuang, Johannes Kopf, and Jia-Bin Huang. Robust dynamic radiance fields. In *Proc. Computer Vision and Pattern Recognition (CVPR)*, pages 13–23, 2023. 1, 2, 4, 6
- [36] Xuan Luo, Jia-Bin Huang, Richard Szeliski, Kevin Matzen, and Johannes Kopf. Consistent video depth estimation. *ACM Transactions on Graphics (ToG)*, 39(4):71–1, 2020. 1, 2
- [37] Thomas Müller, Alex Evans, Christoph Schied, and Alexander Keller. Instant neural graphics primitives with a multiresolution hash encoding. *ACM Trans. Graph.*, 41(4):102:1–102:15, 2022. 6
- [38] Raul Mur-Artal, Jose Maria Martinez Montiel, and Juan D Tardos. Orb-slam: a versatile and accurate monocular slam system. *IEEE transactions on robotics*, 31(5):1147–1163, 2015. 2
- [39] Richard A Newcombe, Steven J Lovegrove, and Andrew J Davison. Dtam: Dense tracking and mapping in real-time. In *Proc. Int. Conf. on Computer Vision (ICCV)*, pages 2320–2327. IEEE, 2011. 2
- [40] Keunhong Park, Utkarsh Sinha, Jonathan T Barron, Sofien Bouaziz, Dan B Goldman, Steven M Seitz, and Ricardo Martin-Brualla. Nerfies: Deformable neural radiance fields. In *Proc. Computer Vision and Pattern Recognition (CVPR)*, pages 5865–5874, 2021. 2
- [41] Keunhong Park, Utkarsh Sinha, Peter Hedman, Jonathan T Barron, Sofien Bouaziz, Dan B Goldman, Ricardo Martin-Brualla, and Steven M Seitz. Hypernerf: A higher-dimensional representation for topologically varying neural radiance fields. *arXiv preprint arXiv:2106.13228*, 2021. 2
- [42] Keunhong Park, Philipp Henzler, Ben Mildenhall, Jonathan T Barron, and Ricardo Martin-Brualla. Camp: Camera preconditioning for neural radiance fields. *ACM Transactions on Graphics (TOG)*, 42(6):1–11, 2023. 2
- [43] F. Perazzi, J. Pont-Tuset, B. McWilliams, L. Van Gool, M. Gross, and A. Sorkine-Hornung. A benchmark dataset and evaluation methodology for video object segmentation. In *Computer Vision and Pattern Recognition*, 2016. 8
- [44] Luigi Piccinelli, Yung-Hsu Yang, Christos Sakaridis, Mattia Segu, Siyuan Li, Luc Van Gool, and Fisher Yu. UniDepth: Universal monocular metric depth estimation. In *Proc. Computer Vision and Pattern Recognition (CVPR)*, 2024. 2, 4, 12, 13
- [45] Marc Pollefeys, Luc Van Gool, Maarten Vergauwen, Frank Verbiest, Kurt Cornelis, Jan Tops, and Reinhard Koch. Visual modeling with a hand-held camera. *International Journal of Computer Vision*, 59:207–232, 2004. 2
- [46] Marc Pollefeys, David Nistér, J-M Frahm, Amir Akbarzadeh, Philippos Mordohai, Brian Clipp, Chris Engels, David Gallup, S-J Kim, Paul Merrell, et al. Detailed real-time urban 3d reconstruction from video. *International Journal of Computer Vision*, 78:143–167, 2008. 2
- [47] René Ranftl, Katrin Lasinger, David Hafner, Konrad Schindler, and Vladlen Koltun. Towards robust monocular depth estimation: Mixing datasets for zero-shot cross-dataset transfer. *IEEE transactions on pattern analysis and machine intelligence*, 44(3):1623–1637, 2020. 2
- [48] René Ranftl, Alexey Bochkovskiy, and Vladlen Koltun. Vision transformers for dense prediction. In *Proc. Computer Vision and Pattern Recognition (CVPR)*, pages 12179–12188, 2021. 2
- [49] Hippolyt Ritter, Aleksandar Botev, and David Barber. A scalable laplace approximation for neural networks. In *6th international conference on learning representations, ICLR 2018-conference track proceedings*. International Conference on Representation Learning, 2018. 5
- [50] Saurabh Saxena, Charles Herrmann, Junhwa Hur, Abhishek Kar, Mohammad Norouzi, Deqing Sun, and David J Fleet. The surprising effectiveness of diffusion models for optical flow and monocular depth estimation. *Advances in Neural Information Processing Systems*, 36, 2024. 2
- [51] Mohamed Sayed, John Gibson, Jamie Watson, Victor Prisacariu, Michael Firman, and Clément Godard. Simplerecon: 3d reconstruction without 3d convolutions. In *European Conference on Computer Vision*, pages 1–19. Springer, 2022. 5
- [52] Johannes L Schonberger and Jan-Michael Frahm. Structure-from-motion revisited. In *Proceedings of the IEEE conference on computer vision and pattern recognition*, pages 4104–4113, 2016. 2, 7, 12
- [53] Johannes L Schönberger, Enliang Zheng, Jan-Michael Frahm, and Marc Pollefeys. Pixelwise view selection for unstructured

- multi-view stereo. In *Computer Vision–ECCV 2016: 14th European Conference, Amsterdam, The Netherlands, October 11–14, 2016, Proceedings, Part III 14*, pages 501–518. Springer, 2016. [12](#)
- [54] Jiahao Shao, Yuanbo Yang, Hongyu Zhou, Youmin Zhang, Yujun Shen, Matteo Poggi, and Yiyi Liao. Learning temporally consistent video depth from video diffusion priors. *arXiv preprint arXiv:2406.01493*, 2024. [2](#)
- [55] Shihao Shen, Yilin Cai, Wenshan Wang, and Sebastian Scherer. Dytanvo: Joint refinement of visual odometry and motion segmentation in dynamic environments. In *2023 IEEE International Conference on Robotics and Automation (ICRA)*, pages 4048–4055. IEEE, 2023. [2](#)
- [56] Noah Snavely, Steven M Seitz, and Richard Szeliski. Photo tourism: exploring photo collections in 3d. In *ACM siggraph 2006 papers*, pages 835–846. 2006. [2](#)
- [57] Chris Sweeney, Aleksander Holynski, Brian Curless, and Steve M Seitz. Structure from motion for panorama-style videos. *arXiv preprint arXiv:1906.03539*, 2019. [2](#)
- [58] Chengzhou Tang and Ping Tan. Ba-net: Dense bundle adjustment network. *arXiv preprint arXiv:1806.04807*, 2018. [2](#)
- [59] Zachary Teed and Jia Deng. Raft: Recurrent all-pairs field transforms for optical flow. In *Computer Vision–ECCV 2020: 16th European Conference, Glasgow, UK, August 23–28, 2020, Proceedings, Part II 16*, pages 402–419. Springer, 2020. [5](#), [12](#)
- [60] Zachary Teed and Jia Deng. Droid-slam: Deep visual slam for monocular, stereo, and rgb-d cameras. *Advances in neural information processing systems*, 34:16558–16569, 2021. [1](#), [2](#), [7](#)
- [61] Zachary Teed, Lahav Lipson, and Jia Deng. Deep patch visual odometry. *Advances in Neural Information Processing Systems*, 36, 2024. [2](#)
- [62] Bill Triggs, Philip F McLauchlan, Richard I Hartley, and Andrew W Fitzgibbon. Bundle adjustment—a modern synthesis. In *Vision Algorithms: Theory and Practice: International Workshop on Vision Algorithms Corfu, Greece, September 21–22, 1999 Proceedings*, pages 298–372. Springer, 2000. [2](#), [3](#)
- [63] Shinji Umeyama. Least-squares estimation of transformation parameters between two point patterns. *IEEE Transactions on Pattern Analysis & Machine Intelligence*, 13(04):376–380, 1991. [7](#)
- [64] Jianyuan Wang, Nikita Karaev, Christian Rupprecht, and David Novotny. Vggsfm: Visual geometry grounded deep structure from motion. In *Proceedings of the IEEE/CVF Conference on Computer Vision and Pattern Recognition*, pages 21686–21697, 2024. [2](#)
- [65] Qianqian Wang, Vickie Ye, Hang Gao, Jake Austin, Zhengqi Li, and Angjoo Kanazawa. Shape of motion: 4d reconstruction from a single video. *arXiv preprint arXiv:2407.13764*, 2024. [2](#), [4](#), [6](#)
- [66] Sen Wang, Ronald Clark, Hongkai Wen, and Niki Trigoni. Deepvo: Towards end-to-end visual odometry with deep recurrent convolutional neural networks. In *2017 IEEE international conference on robotics and automation (ICRA)*, pages 2043–2050. IEEE, 2017. [2](#)
- [67] Shuzhe Wang, Vincent Leroy, Yohann Cabon, Boris Chidlovskii, and Jerome Revaud. Dust3r: Geometric 3d vision made easy. In *Proc. Computer Vision and Pattern Recognition (CVPR)*, pages 20697–20709, 2024. [2](#), [6](#)
- [68] Shizun Wang, Xingyi Yang, Qihong Shen, Zhenxiang Jiang, and Xinchao Wang. Gflow: Recovering 4d world from monocular video. *arXiv preprint arXiv:2405.18426*, 2024. [2](#)
- [69] Wenshan Wang, DeLong Zhu, Xiangwei Wang, Yaoyu Hu, Yuheng Qiu, Chen Wang, Yafei Hu, Ashish Kapoor, and Sebastian Scherer. Tartanair: A dataset to push the limits of visual slam. 2020. [6](#), [14](#)
- [70] Yiran Wang, Min Shi, Jiaqi Li, Zihao Huang, Zhiguo Cao, Jianming Zhang, Ke Xian, and Guosheng Lin. Neural video depth stabilizer. In *Proc. Computer Vision and Pattern Recognition (CVPR)*, pages 9466–9476, 2023. [2](#)
- [71] Rundi Wu, Ruiqi Gao, Ben Poole, Alex Trevithick, Changxi Zheng, Jonathan T Barron, and Aleksander Holynski. Cat4d: Create anything in 4d with multi-view video diffusion models. *arXiv preprint arXiv:2411.18613*, 2024. [2](#)
- [72] Lihe Yang, Bingyi Kang, Zilong Huang, Xiaogang Xu, Jiashi Feng, and Hengshuang Zhao. Depth anything: Unleashing the power of large-scale unlabeled data. In *CVPR*, 2024. [2](#), [4](#), [12](#), [13](#)
- [73] Lihe Yang, Bingyi Kang, Zilong Huang, Zhen Zhao, Xiaogang Xu, Jiashi Feng, and Hengshuang Zhao. Depth anything v2. *arXiv preprint arXiv:2406.09414*, 2024. [2](#), [6](#)
- [74] Nan Yang, Lukas von Stumberg, Rui Wang, and Daniel Cremers. D3vo: Deep depth, deep pose and deep uncertainty for monocular visual odometry. In *Proc. Computer Vision and Pattern Recognition (CVPR)*, pages 1281–1292, 2020. [2](#), [12](#)
- [75] Wei Yin, Jianming Zhang, Oliver Wang, Simon Niklaus, Long Mai, Simon Chen, and Chunhua Shen. Learning to recover 3d scene shape from a single image. In *Proc. Computer Vision and Pattern Recognition (CVPR)*, pages 204–213, 2021. [2](#)
- [76] Wei Yin, Chi Zhang, Hao Chen, Zhipeng Cai, Gang Yu, Kaixuan Wang, Xiaozhi Chen, and Chunhua Shen. Metric3d: Towards zero-shot metric 3d prediction from a single image. In *Proc. Computer Vision and Pattern Recognition (CVPR)*, pages 9043–9053, 2023. [2](#)
- [77] Junyi Zhang, Charles Herrmann, Junhwa Hur, Varun Jampani, Trevor Darrell, Forrester Cole, Deqing Sun, and Ming-Hsuan Yang. MonST3R: A simple approach for estimating geometry in the presence of motion. *arXiv preprint arXiv:2410.03825*, 2024. [1](#), [2](#), [6](#), [7](#), [8](#)
- [78] Zhoutong Zhang, Forrester Cole, Richard Tucker, William T Freeman, and Tali Dekel. Consistent depth of moving objects in video. *ACM Transactions on Graphics (ToG)*, 40(4):1–12, 2021. [1](#), [2](#)
- [79] Zhoutong Zhang, Forrester Cole, Zhengqi Li, Michael Rubinstein, Noah Snavely, and William T Freeman. Structure and motion from casual videos. In *European Conference on Computer Vision*, pages 20–37. Springer, 2022. [1](#), [2](#), [5](#), [6](#), [7](#), [8](#), [12](#), [13](#), [14](#)
- [80] Wang Zhao, Shaohui Liu, Hengkai Guo, Wenping Wang, and Yong-Jin Liu. Particlesfm: Exploiting dense point trajectories for localizing moving cameras in the wild. In *European Conference on Computer Vision*, pages 523–542. Springer, 2022. [1](#), [2](#), [6](#)

A. Implementation Details

A.1. System Overview

Figure 9 shows an overview of our MegaSaM system. We separate the problem of camera and scene structure estimation into two stages, in the spirit of a conventional SfM pipeline [52, 53]. In particular, we first estimate camera poses $\hat{\mathbf{G}}$, focal length \hat{f} and low-resolution disparity $\hat{\mathbf{d}}$ from the input monocular video through differentiable Bundle Adjustment (BA), where we initialize $\hat{\mathbf{d}}$ with monocular depth maps predicted from off-the-shelf models [44, 72]. In the second consistent video depth estimation phase, we fix estimated camera parameters and perform first-order optimization over video depth and uncertainty maps by enforcing flow and depth losses induced by pairwise 2D optical flows.

A.2. Framework and Architecture

We follow DROID-SLAM [59] for feature extraction, correlation feature construction, and perform iterative BA updates through flow, confidence, motion probability predictions. Each input to the model is a pair of video frames (I_i, I_j).

Feature extraction. We use context and feature encoders to encode each input video frame into two different low-resolution feature maps at $\frac{1}{8}$ resolution of the input image, as shown in Figure 11.

Correlation feature construction. The correlation layer constructs a 4D correlation volume from the features encoded from an image pair, and each entry of the volume contains inner product of one pairs of feature vectors from the image pair.

Iterative updates. During each iterative BA step k , we update camera parameters and low-resolution disparity through flow, confidence and motion probability prediction. In particular, we first pretrain F on synthetic video data (ego-motion pretraining in the main paper) to learn to predict flows and corresponding flow confidence, as shown by the gray blocks in Figure 10. In the second dynamic finetuning phase, we freeze the parameters of F and finetune the motion module F_m to predict extra object motion probability maps conditioned on the features from the ConvRGU, as shown in the blue blocks in Figure 10. Within the motion module, we first perform 2D spatial average pooling to provide the model with global spatial information; we then perform average pooling along the time axis to fuse information from I_i and all its neighboring keyframes I_j (where $j \in \mathcal{N}(i)$).

A.3. Consistent Video Depth Optimization

Recall, from Section 3.3 of our main paper, that we follow CasualSAM [79] to estimate consistent video depth by performing an additional first-order optimization on video disparity \hat{D}_i along with per-frame aleatoric uncertainty maps \hat{M}_i . Instead of jointly optimizing camera parameters and

scene structure as in CasualSAM, however, we fix camera parameters as done in conventional SfM pipelines like COLMAP [52, 53].

Our objective consists of three main cost functions:

$$\mathcal{C}_{\text{cvd}} = w_{\text{flow}}\mathcal{C}_{\text{flow}} + w_{\text{temp}}\mathcal{C}_{\text{temp}} + w_{\text{prior}}\mathcal{C}_{\text{prior}} \quad (12)$$

We treat object motion in the video as the heteroscedastic aleatoric uncertainty of the flow reprojection and depth consistency error [23], and assume the underlying noise is Laplacian [74]. Specifically, for each selected pair (I_i, I_j), flow reprojection loss $\mathcal{C}_{\text{flow}}$ compares l_1 loss weighted by the uncertainty \hat{M}_i between flows $\text{flow}_{i \rightarrow j}$ from an off-the-shelf flow estimator [59] and the correspondences \mathbf{u}_{ij} induced by our estimated camera motion and disparity through a multi-view constraint:

$$\mathcal{C}_{\text{flow}}^{i \rightarrow j} = \hat{M}_i \|\mathbf{u}_{ij} - \mathbf{p}_i, \text{flow}_{i \rightarrow j}(\mathbf{p}_i)\|_1 + \log\left(\frac{1}{\hat{M}_i}\right), \quad (13)$$

$$\mathbf{u}_{ij} = \pi\left(\hat{\mathbf{G}}_{ij} \circ \pi^{-1}(\mathbf{p}_i, \hat{D}_i, K^{-1}), K\right) \quad (14)$$

$\mathcal{C}_{\text{temp}}$ is an uncertainty weighted temporal depth loss that encourages pixel disparity to be temporally consistent according to estimated 2D optical flow:

$$\mathcal{C}_{\text{temp}}^{i \rightarrow j} = \hat{M}_i \delta\left(\mathbf{P}_z^{i \rightarrow j}, \hat{D}_j(\mathbf{p} + \text{flow}_{i \rightarrow j}(\mathbf{p}))\right) + \log\left(\frac{1}{\hat{M}_i}\right)$$

$$\delta(a, b) = \|\max(\frac{a}{b}, \frac{b}{a})\|_1$$

$$\mathbf{P}_z^{i \rightarrow j} = (D_i(\mathbf{p})\mathbf{R}_{i \rightarrow j}\mathbf{K}^{-1}\mathbf{p} + \mathbf{t}_{i \rightarrow j})_{[z]} \quad (15)$$

$\mathbf{R}_{i \rightarrow j}$ and $\mathbf{t}_{i \rightarrow j}$ are relative camera rotation and translation between I_i and I_j ; $_{[z]}$ is an operator that retrieve the third component of the 3D point vector (i.e. z value).

$\mathcal{C}_{\text{prior}}$ is a depth prior loss that stops the final estimated video disparity from drifting too much from the initial estimate from the mono-depth network, and it consists of three losses:

$$\mathcal{C}_{\text{prior}} = \mathcal{C}_{\text{si}} + w_{\text{grad}}\mathcal{C}_{\text{grad}} + w_{\text{normal}}\mathcal{C}_{\text{normal}} \quad (16)$$

The scale-invariant depth loss \mathcal{C}_{si} computes the mean square error of the difference among all pairs between optimized log-disparity $\log \hat{D}_i$ and initial log-disparity from the metric-aligned mono-depth prediction $\log D_i^{\text{align}}$.

$$\mathcal{C}_{\text{si}} = \frac{1}{n} \sum_{(\mathbf{p})} (R(\mathbf{p}))^2 - \frac{1}{n^2} \left(\sum_{(\mathbf{p})} R(\mathbf{p}) \right)^2$$

$$R_i = \log(\hat{D}_i) - \log(D_i^{\text{align}}). \quad (17)$$

$\mathcal{C}_{\text{grad}}$ is a multi-scale scale-invariant gradient matching term [30], which computes l_1 difference between estimated log disparity gradients and initial log-disparity gradients

$$\mathcal{C}_{\text{grad}} = \frac{1}{n} \sum_s w_{\nabla}^s(\mathbf{p}) \sum_{\mathbf{p}} (|\nabla_x R^s(\mathbf{p})| + |\nabla_y R^s(\mathbf{p})|)$$

$$w_{\nabla}^s(\mathbf{p}) = 1 - \exp(-\beta_{\nabla}(\nabla_x R^s(\mathbf{p}) + \nabla_y R^s(\mathbf{p}))) \quad (18)$$

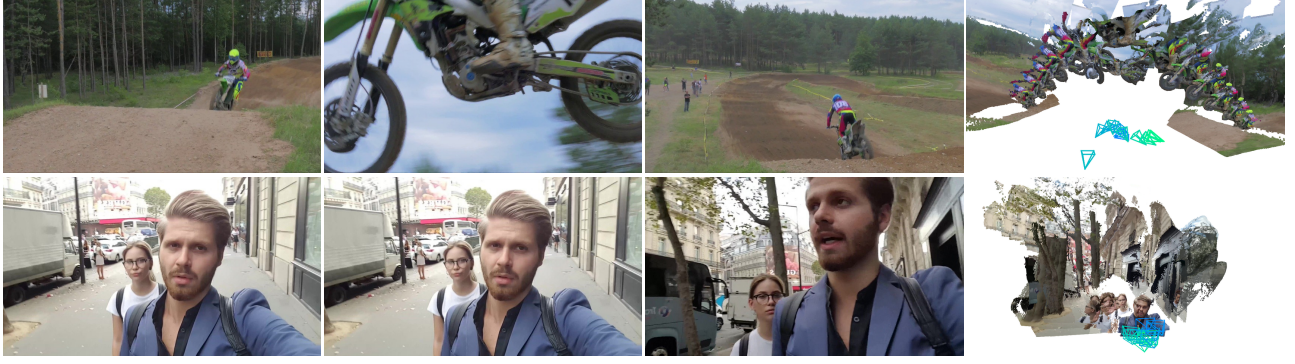


Figure 8. **Limitations.** We visualize three reference video frames on the left and their corresponding estimated camera paths and reconstruction on the right. Our method can lose tracks in cases where a moving object dominates the entire videos (top row). Our approach can also struggle in cases where object motion and camera motion are colinear, such as the selfie video in the bottom row.

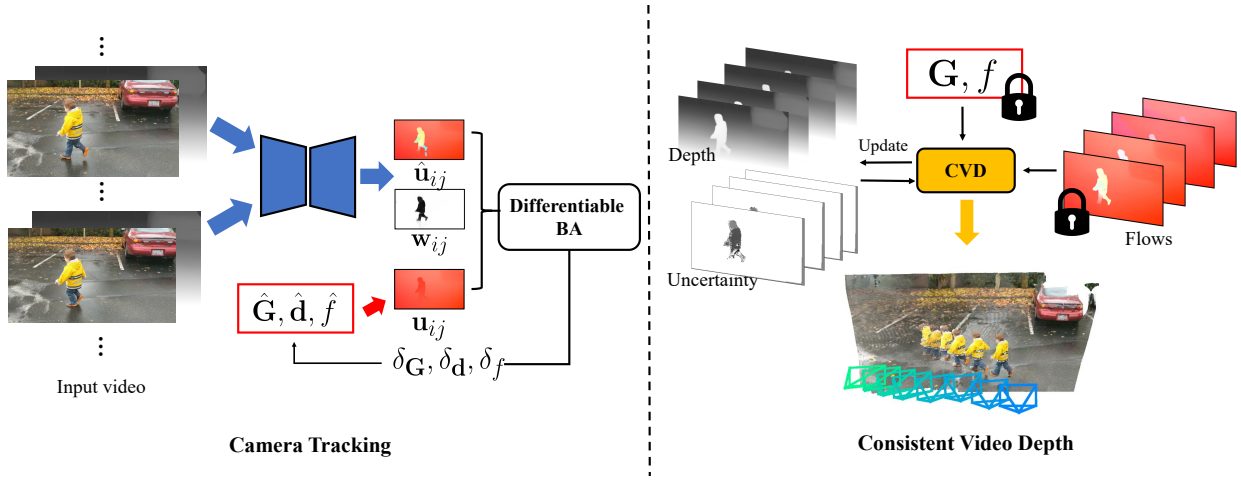


Figure 9. **System overview.** **Left:** we estimate camera poses, focal length and low-resolution disparity maps from the input monocular video through differentiable Bundle Adjustment (BA): the network iteratively updates these state variables by learning to predict low-resolution flow $\hat{\mathbf{u}}_{ij}$, confidence, and movement probability maps \mathbf{w}_{ij} and minimize weighted reprojection error between predicted flow $\hat{\mathbf{u}}_{ij}$ and flow induced by ego-motion \mathbf{u}_{ij} . We also initialize estimated disparity with mono-depth predicted from off-the-shelf models [44, 72]. **Right:** we fix estimated camera parameters and perform first-order global optimization over video depth and corresponding uncertainty parameters by minimizing flow and depth losses through pairwise 2D optical flows.

where $R^s(\mathbf{p})$ is log-depth difference map at pixel position \mathbf{p} and scale s . In other words, we only apply multi-scale gradient matching loss to pixels where the current estimated disparity deviates significantly from the original mono-depth.

C_{normal} is a surface normal loss that encourages that normal $\hat{\mathbf{N}}(\mathbf{p})$ derived from estimated disparity to be close to the surface normal $\mathbf{N}^{\text{align}}$ derived from the initial metric-aligned monocular disparity:

$$C_{\text{normal}} = \sum_{\mathbf{p}} 1 - \hat{\mathbf{N}}(\mathbf{p}) \cdot \mathbf{N}^{\text{align}}(\mathbf{p}) \quad (19)$$

We set $w_{\text{grad}} = 1, w_{\text{normal}} = 4, \beta_{\nabla} = 5$ throughout our experiments. We simply choose image pairs (I_i, I_j) from a set of fixed intervals following prior work [79]: $j \in (i + 1, i + 2, i + 4, i + 8, i + 15)$. During optimization,

we initialize the disparity variables from the metric-aligned monocular depth by combining estimates from off-the-shelf modules as described in the main paper [44, 72], and we initialize the uncertainty map with object motion probability maps predicted from our camera tracking module. The optimization first conducts a “warm-up” phase for 100 steps by fixing the video disparity variables and optimizing the per-frame uncertainty map, per-frame scale, shift variables using the aforementioned losses. The disparity maps and uncertainty maps are then optimized together under the aforementioned losses for another 400 steps.

A.4. Additional Details

Training Losses. We supervise our network using a combination of pose loss and flow loss. The flow loss is applied

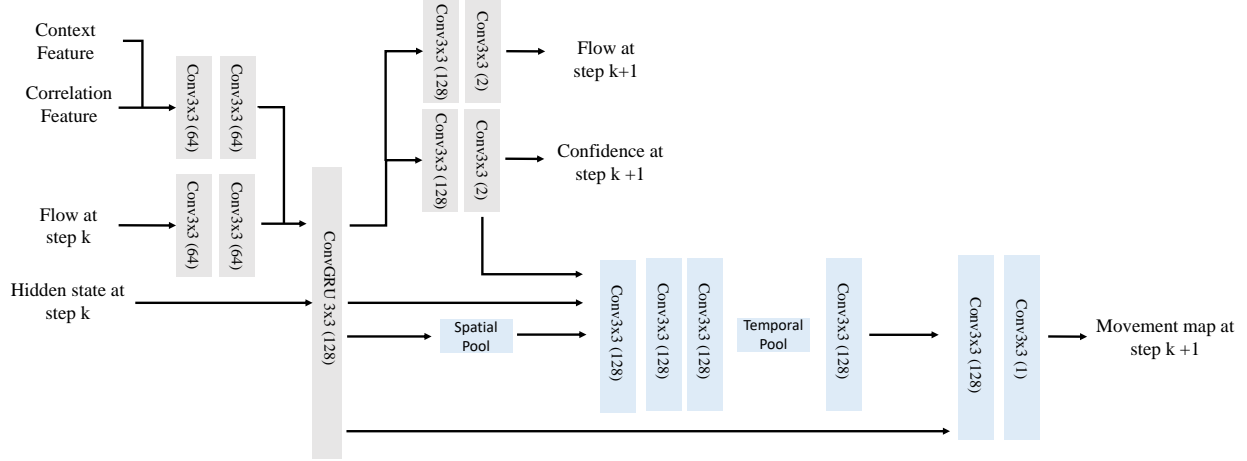


Figure 10. Architecture of flow, confidence and movement map predictor. The gray blocks belong to the network F for flow and confidence prediction, and the blue blocks belong to the network F_m for object movement map prediction. In the first stage, we perform ego-motion pretraining for F . In the second stage, we perform dynamic fine-tuning for F_m while fixing the parameters of F .

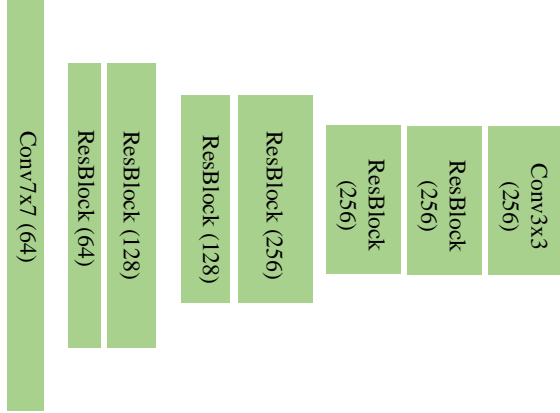


Figure 11. Architecture of the feature and context encoders. Both encoders extract low-resolution features from input video frames at $\frac{1}{8}$ of the original resolution.

to pairs of adjacent frames. We compute the optical flow induced by the predicted depth and poses and the flow induced by the ground truth depth and poses. The loss is taken to be the average l2 distance between the two flow fields.

Given a set of ground truth poses $\{\mathbf{T}_i\}_{i=1}^N$ and predicted poses $\{\mathbf{G}_i\}_{i=1}^N$, the pose loss is taken to be the distance between the ground truth and predicted poses, $\mathcal{L}_{pose} = \sum_i \|\text{Log}_{SE(3)}(\mathbf{T}_i^{-1} \cdot \mathbf{G}_i)\|_2$. We apply the losses to the output of every BA iteration with exponentially increasing weight using $\gamma = 0.9^k$, where k indicates the k^{th} BA iterations.

Training and Inference Details In our two-stage training scheme, we first pretrain our model on synthetic data of

static scenes, which include 163 scenes from TartanAir [69] and 5K videos from static Kubric [15]. In the second stage, we finetune motion module F_m on 11K dynamic videos from Kubric [15]. Each training example consists of a 7-frame video sequence. We first precompute a distance matrix between each pair of video frame based on the average ego-motion induced flow magnitude. We then dynamically generate a training sequence according to the constructed distance matrix, we randomly sample each frame such that average flow between them is between 0.5px and 64px.

Within the camera tracking module, we normalize video disparity \hat{d} such that its 98 percentile is 2; we also normalize focal length by dividing it by the input image resolution within every the bundle adjustment stage.

B. Limitations

Despite excellent performance on a variety of in-the-wild videos, we observe that our approach can fail in extremely challenging scenarios, similar to findings from prior work [79]. For instance, camera tracking fails if moving objects dominate the entire image or if there is nothing for the system to track reliably, as shown in the first row of Fig. 8. Furthermore, our approach also struggles on dynamic videos where camera motion and object motion are colinear, as shown in the second row of Fig. 8.